



**HAL**  
open science

## Periodic nanoporous inorganic patterns directly made by self-ordering of cracks

Mateusz Odziomek, Fanny Thorimbert, Cedric Boissiere, Glenna L. Drisko,  
Stephane Parola, Clément Sanchez, Marco Faustini

► **To cite this version:**

Mateusz Odziomek, Fanny Thorimbert, Cedric Boissiere, Glenna L. Drisko, Stephane Parola, et al..  
Periodic nanoporous inorganic patterns directly made by self-ordering of cracks. *Advanced Materials*,  
2022, 34 (36), pp.2204489. 10.1002/adma.202204489 . hal-03735804

**HAL Id: hal-03735804**

**<https://hal.science/hal-03735804v1>**

Submitted on 27 Jul 2022

**HAL** is a multi-disciplinary open access archive for the deposit and dissemination of scientific research documents, whether they are published or not. The documents may come from teaching and research institutions in France or abroad, or from public or private research centers.

L'archive ouverte pluridisciplinaire **HAL**, est destinée au dépôt et à la diffusion de documents scientifiques de niveau recherche, publiés ou non, émanant des établissements d'enseignement et de recherche français ou étrangers, des laboratoires publics ou privés.

## Periodic nanoporous inorganic patterns directly made by self-ordering of cracks

*Mateusz Odziomek, Fanny Thorimbert, Cedric Boissiere, Glenna L. Drisko, Stephane Parola, Clement Sanchez and Marco Faustini\**

Dr. M. Odziomek, F. Thorimbert, Dr. C. Boissiere, Prof. C. Sanchez, Dr. M. Faustini

Sorbonne Université, CNRS, Collège de France, UMR 7574, Chimie de la Matière Condensée de Paris, F-75005 Paris, France.

E-mail: marco.faustini@sorbonne-universite.fr

Dr. M. Odziomek

Université de Paris, ITODYS, CNRS, UMR 7086, 15 rue J-A de Baïf, F-75013 Paris, France

Dr. G. L. Drisko

CNRS, Univ. Bordeaux, Bordeaux INP, ICMCB, UMR 5026, Pessac, F-33600 France

Prof. S. Parola,

Ecole Normale Supérieure de Lyon, CNRS UMR 5182, Université Lyon 1, Laboratoire de Chimie, 46 allée d'Italie, F69364 Lyon, France

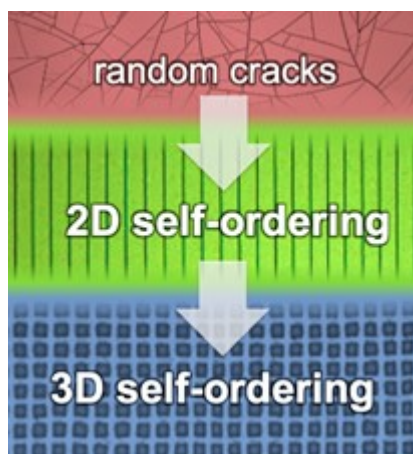
Keywords: porous films, crack, patterning, inorganic, photonics

Solution-processed inorganic nanoporous films are key components for the vast spectrum of applications ranging from dew harvesting to solar cells. Shaping them into complex architectures required for advanced functionality, often need time-consuming or expensive fabrication. In this work,

This article has been accepted for publication and undergone full peer review but has not been through the copyediting, typesetting, pagination and proofreading process, which may lead to differences between this version and the [Version of Record](#). Please cite this article as [doi: 10.1002/adma.202204489](https://doi.org/10.1002/adma.202204489).

we show how crack formation is harnessed to pattern porous inorganic films in a single step and without using lithography. We developed aqueous ink formulations that, in the presence of polymeric latexes, enable evaporation-induced, defect-free periodic arrays of cracks with tunable dimensions over several centimeters. The ink formulation strategy was generalized to more than ten inorganic materials including simple and binary porous oxide and metallic films covering a whole spectrum of properties including insulator, photocatalytic, electrocatalytic, conductive or electrochromic materials. Notably, this approach enables three-dimensional self-assembly of cracks by stacking several layers of different compositions, yielding periodic assemblies of polygonal shapes and Janus-type patterns. The crack patterned periodic arrays of nanoporous TiO<sub>2</sub> diffract light, and are used as temperature-responsive diffraction grating sensors. More broadly, this method represents a unique example of self-assembly process leading to long-range order (over several cm) in a robust and controlled way.

#### Table of Contents



Mateusz Odziomek, Fanny Thorimbert, Cedric Boissiere, Glenna L. Drisko, Stephane Parola, Clement Sanchez and Marco Faustini\*

**Periodic nanoporous inorganic patterns directly made by self-ordering of cracks**

Patterning nanoporous inorganic films by lithography remains a challenge for their integration in functional devices. Liquid deposition of aqueous inks can form patterns via self-ordering of cracks over several cm in both 2D and 3D. The method is chemically versatile and is shown to successfully pattern more than ten functional materials. Periodic arrays of cracks then serve as photonic sensors.

## 1. Introduction

Nanoporous inorganic films are the cornerstone of high-tech applications like sensitized solar cells,<sup>[1,2]</sup> photo- or electrocatalysis,<sup>[3,4]</sup> sensing,<sup>[5]</sup> photonics,<sup>[6,7]</sup> wetting<sup>[8–10]</sup> or microelectronics.<sup>[11,12]</sup> Nevertheless, their fabrication is often complicated and requires additional patterning of the films for integration in functional devices. In the vast majority of cases, structured films are produced using bottom-up approaches through a liquid deposition followed by thermal treatment.<sup>[13–15]</sup> While soft-chemistry was combined with lithography in some cases,<sup>[16]</sup> developing low-cost and large-scale patterning methods remains an important frontier that would facilitate the lab-to market transition. In this regard, methods based on self-assembly (stick-slip,<sup>[17,18]</sup> wrinkling,<sup>[19]</sup> colloidal lithography<sup>[20]</sup>) are very promising but they suffer from limited control over pattern complexity and long-range ordering.

An alternative method, having a higher degree of control over patterning parameters is to use crack formation. Patterning through crack engineering was initially proposed by Nam *et al* for SiN films<sup>[21]</sup> and further extended to polymeric materials.<sup>[22]</sup> Crack nucleation and propagation must be precisely controlled, requiring the prefabrication of defects (notches) on the substrate, which act to concentrate stress. The subsequent film contraction due to either cooling or drying generates large stress at the notch.<sup>[21–24]</sup> Even though such a method allows for precise control over crack nucleation and further propagation, it typically employs lithographic techniques for pre-patterning.<sup>[25]</sup> An alternative is the formation of the spontaneous ordering of cracks in evaporating colloidal droplets. In certain conditions, it has been observed that cracks propagate perpendicularly to the evaporation front forming arrays of radial cracks with relatively uniform spacing. This spontaneous ordering of cracks occurs only upon specific drying conditions of colloidal systems. The origin of the formation of uniform crack patterns upon directional drying of latex colloidal solution has been described in the seminal work of Allain and Limat.<sup>[26]</sup> By controlling the evaporation front and the processing, colloidal films with ordered arrays of radial or linear cracks could be obtained.<sup>[27,28]</sup> Despite the

attractivity of this approach, several challenges still stand. (i) In terms of composition, crack self-ordering has mainly been demonstrated in rather simple, non-functional colloidal films made of polymeric latex or silica particles. While these films could be used as masks to transfer the pattern to other materials (gold, perovskite), this requires multi-steps fabrication schemes (like in the case of lithographic pre-patterning).<sup>[27,28]</sup> In only one example, the approach was extended to Metal Organic Frameworks colloidal films, yet characterized by disordered secondary cracks leading to defective crack patterns.<sup>[29]</sup> (ii) Another limitation of the approach is the limited variety of morphological control in terms of the geometry and shape of the patterns: previous examples of self-ordering cracks exclusively lead to arrays of grooves. (iii) In order to compete with current lithographic techniques, the crack self-ordering should be reproduced without defects over relatively large surfaces.

Herein we tackle all the aforementioned challenges by developing aqueous-based ink formulations compatible with several meniscus-guided deposition techniques (such as dip- or blade-coating) to form a wide range of inorganic nanoporous films with periodic crack patterns propagating homogeneously without defects over several centimetres. The inks are composed of polymeric latexes colloids with an engineered surface and various inorganic precursors. The polymeric colloids act as both crack-directing agents and templates to form patterned inorganic porous materials. Indeed after deposition, further thermal treatment causes crystallization of the inorganic phase and concomitant removal of pore-forming polymeric latexes. This method is highly versatile and generalized to more than ten inorganic materials, including simple and binary porous oxide and metallic films. The process is robust and mitigates typical problems in co-deposition of inorganic precursors and colloidal templates.<sup>[30,31]</sup> Thanks to special design of latex surface, the inorganic precursors do not induce instabilities in the ink. Additionally, this approach can be extended toward three dimensional crack self-ordering of more complex geometries and periodic assemblies of polygonal shapes, with heterostructured Janus features. We exploit the long-range order of patterned surfaces to fabricate photonic porous gratings, responsive to vapors and temperature changes.

## 2. Results

### 2.1. Crack ordering in titania films

To illustrate our method, we first detail the example of nanoporous titania, a relevant material for applications in solar-cells<sup>[32,33]</sup> and photocatalysis<sup>[34,35]</sup>. The overall process consists of three steps: (i) preparation of the ink composed of polymeric latex colloids and the inorganic precursor; (ii) deposition of the ink on the substrate and simultaneous crack patterning; (iii) thermal treatment to remove the template and to induce the crystallization of the inorganic phase (**Figure 1**). The main challenge is related to the ink formulation. The ink needs to enable crack self-ordering (the importance of colloids on crack self-ordering is further discussed in **supplementary note 1** in SI) and be stable during the course of the deposition. Therefore, we synthesized polystyrene (PS) latex colloids having steric stabilization provided by a nonionic surfactant (Pluronic F127) (Figure S1). They are remarkably stable in different environments, in contrast to regular latex particles stabilized by ionic surfactants, which are sensitive to any change of solvent quality or addition of ionic species. Beyond stability, we find that using Pluronic-stabilized latex particles give the best results in term of self-ordering of cracks in presence of inorganic precursors (**supplementary note 2** in SI and Figure S2). In the case of titania, the choice of the precursors was particularly difficult due to their sensitivity toward the water. Among the various precursors, titanium alkoxides stabilized with acetylaceton<sup>[36]</sup> provided the best results (**see supplementary note 3** in SI and Figure S3). The second step corresponds to the simultaneous patterning during film deposition. **Figure 1a** displays a sequence of photographs taken during dip-coating deposition of the titania ink on a silicon substrate.

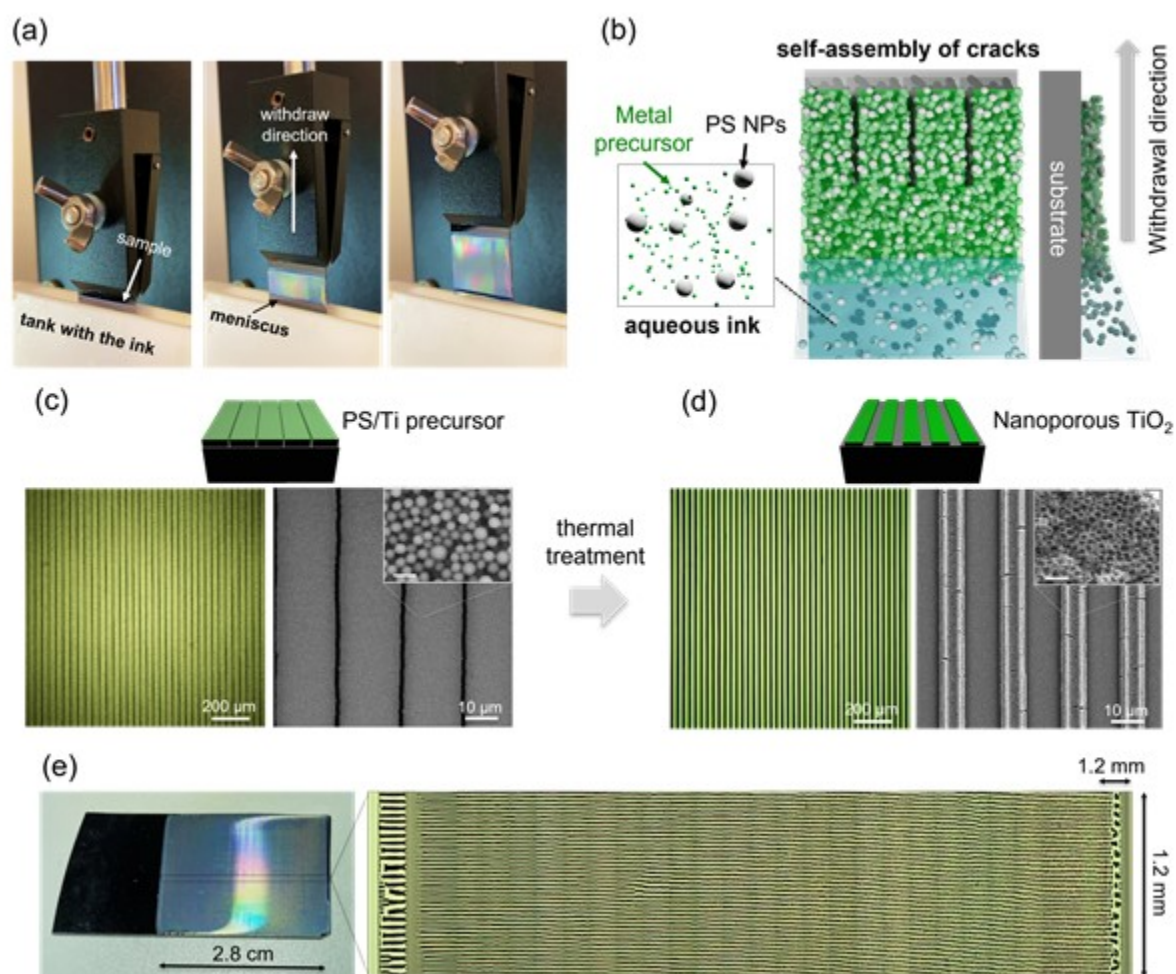


**Figure 1. Direct fabrication of inorganic porous patterns by self-ordering of cracks.** (a) Photographs of the crack self-ordering process during dip-coating. (b) Schematic of the crack formation during deposition by dip-coating of an ink composed of latex particles and an inorganic precursor. (c,d) (upper) Schematic of crack-patterned titania inks with associated (left) optical microscopy and (right) SEM images, of as-deposited (c) and calcined at 450 °C in air (d). Insets show high magnification SEM images of ridges. (e) A photograph of a TiO<sub>2</sub> crack-patterned film after calcination at 450 °C and a compressed optical microscope images of the whole length of the film.

The ink needs to be applied by meniscus-guided deposition techniques (such as dip-coating, blade-coating or drop-casting) in which the timescale for solvent evaporation is shorter than the coating rate (capillary regime) (Figure S4).<sup>[37,38]</sup> The crack self-ordering process is illustrated in the scheme in **Figure 1b** and in the optical microscopy images in Figures S4 and movie S1. During the deposition

process, the latex particles and the inorganic precursor are co-deposited. Dip-coating at low withdrawal speeds (capillary regime) provides directionality in the drying process, wherein the horizontal drying front follows the meniscus at a constant pace determined by the withdrawal speed. In the presence of particles, cracks propagate perpendicularly to the drying front, the direction of maximum stress.<sup>[39]</sup> The importance of colloids for crack self-ordering is further discussed in Supplementary Note 1. The even spacing between cracks results from the competition between stress relaxation near the crack and the accumulation of stress due to enhanced liquid evaporation through the new surfaces formed by the crack. As reported in the literature, these two contributions create maximum stress at a fixed distance.<sup>[26]</sup> The formation of oriented and periodic cracks results in the appearance of iridescent colors over the whole sample that are clearly visible at the macroscopic scale (see photograph and optical microscopy image in **Figure 1e**). It is important to mention that the direct deposition of inorganic precursors without latexes leads to films with disordered and non-directional cracking (Figure S5).

**Figure 1c** shows the self-assembled cracks in an as-deposited film from a titania ink (latex particles + titanium butoxide stabilized with acetylacetonate, denoted in the text as TiOR/PS for simplicity). Scanning electron microscopy (SEM) images unveiled ridges built from randomly close-packed latex particles surrounded by the TiO<sub>2</sub> precursor (**Figure 1c** inset). Examination at higher magnification revealed that titania species (most likely in the form of oxo-clusters)<sup>[40]</sup> condensed primarily in the liquid bridges between two neighbouring latex particles, as commonly seen in the late stages of the drying process (Figure S6). As shown in **Figure 1d**, further thermal treatment decomposes polymeric colloids. Thermal treatment also induces crystallization of the TiO<sub>2</sub> phase, which entails migration of TiO<sub>2</sub> to form a highly porous film that is mainly composed by sub-100 nm macropores (Figure S6).. The unidirectional crack-patterned structure is fully preserved, as indicated in the optical and SEM micrographs shown in **Figure 1d**. The process is robust and accesses large surfaces with a high micropattern quality (Figure S7). The propagating cracks follow their path uniformly over at least several centimeters, displaying no damage from calcination (**Figure 1e**).

There are two critical steps to obtain a uniform micropattern. The first is the formation of cracks during the film deposition, and the second is the transition from hybrid to inorganic film upon calcination. The crucial parameter for both is the ratio between the TiO<sub>2</sub> precursor and latex particles. On the one hand, a content of TiO<sub>2</sub> that is too high affects the cracking process by forming poorly organized cracks, and, on the other hand, a TiO<sub>2</sub>/PS ratio that is too low leads to featureless

films without any pattern after calcination (Figure S8). A specific optimum ratio for TiOR/PS films was determined to be around one mmol of titanium atoms per gram of PS (Figure S8).

The parameters of the micropattern, such as crack spacing and crack width, are rather simple to tune because they depend on the deposition conditions. According to the literature, the crack spacing scales almost linearly with the thickness<sup>[26,27,28]</sup>. For our materials, before calcination, the ratio between crack spacing and thickness is around 3 as determined by analyzing several SEM cross-section micrographs such as in Figure S11. In dip-coating deposition the thickness of the film ( $h$ ) is inversely proportional to the deposition rate ( $u$ ) in the capillary regime as shown in Equation 1.<sup>[38,41,42]</sup>

$$h = k - \quad (1)$$

where  $k$  is a constant characteristic of the solution (that includes the inorganic concentration, the molar weight and the density of the material. the volume fraction of the inorganic material),  $E$  is the evaporation rate and  $L$  is the width of the deposited layer, which doesn't change during the dip-coating process. For a given solution, modifying the withdrawal speed during dip-coating, provides a fine control over the thickness and thus the crack spacing. **Figure 2a** represents the relationship between withdrawal speed and the crack spacing, based on the optical microscopy images of TiOR/PS inks deposited at different speeds (Figure S9) and compared to the crack spacing obtained with pure aqueous latex solution. The presence of the  $\text{TiO}_2$  precursor does not change the crack spacing because of its relatively low concentration in the sol. Above a certain film thickness, produced usually at very low speeds, the film can delaminate in the direction of the cracks (Figure S9). This results from residual stress remaining in the film after cracking and partial drying. In the case of TiOR/PS films, this happens for relatively thick films with crack spacing above  $50 \mu\text{m}$  (withdrawal speeds below  $2 \mu\text{m/s}$ ). On the contrary, cracks become less organized and eventually isolated at faster withdrawal speeds (crack spacing below  $8 \mu\text{m}$ ). It is worth mentioning that the temperature (Figure S10) and the concentration of the ink also have a strong influence on the thickness of the film due to convective assembly, and therefore, also on the crack spacing.

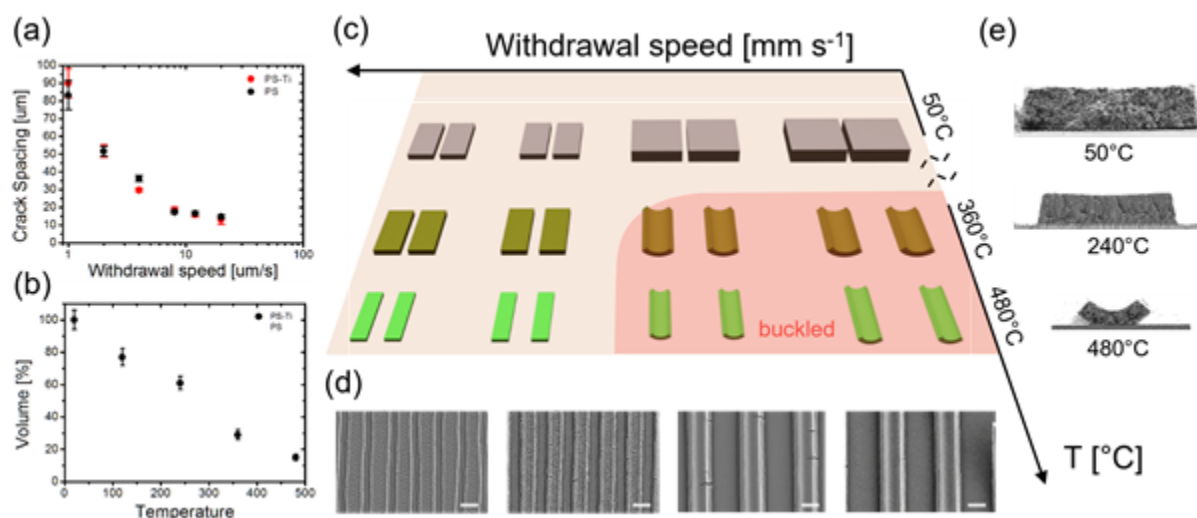


**Figure 2. Tuning the features of crack-patterned TiO<sub>2</sub> films.** (a) The crack spacing as a function of withdrawal speed of TiOR/PS inks (red dots) and pure depositions of PS latexes (black dots) of the same concentration of latex particles (10 wt%) and temperature during deposition (50 °C). (b) The cross-sectional area of the TiOR/PS ridges at different calcination temperatures (expressed as the percentage of the initial volume). (c) Schematic representing the size and shape of the ridges as well as the crack spacing of TiOR/PS films deposited at different speeds and calcined at different temperatures, the proportions of the ridge sizes and distance between them correspond to measured values. (d) SEM images of calcined crack-patterned Titania prepared at different withdrawal speeds: 16, 8, 4, 2 μm s<sup>-1</sup> from left to right, scale bar 15 μm. (e) SEM images of cross-section of TiOR/PS ridges obtained at a withdrawal speed of 4 μm s<sup>-1</sup> at different calcination temperatures.

Calcination not only crystallizes the oxide and removes the latexes, but also entails significant microstructural changes. The contraction as a function of temperature is quantified by measuring the cross-sectional area of the ridges from SEM pictures (**Figure 2e** and S11) and is represented in **Figure 2b**. In addition, the thermal transition has been followed *in situ* and *ex situ* by optical microscopy and *in situ* infrared ellipsometry (Figure S12-14). There are two phenomena responsible for the contraction. First, polymer melting starts at around 110 °C (glass transition temperature) causing slight lateral shrinkage of the ridges and widening crack width (Figure S12a, S13). The film becomes more transparent and less diffusive as a consequence of the pores disappearance and reduced scattering. The melting of polymer and loss of interparticle porosity is further confirmed by

increase of refractive index measured by infrared ellipsometry (Figure S14). Above 300 °C, the polymer decomposes, fostering significant shrinkage and additional strain, leading to partial buckling. The removal of the polymer leaves enormous free space making the inorganic phase highly porous and causing a large drop in refractive index (Figure S14). The convex shaped-ridges are made of porous TiO<sub>2</sub> as shown in **Figures 1d and 3**. This indicates that TiO<sub>2</sub> network develops before or during the polymer melting/decomposition and that it is strong enough to withstand enormous porosity. In fact, ellipsometry measurement of calcined, non-cracked TiO<sub>2</sub> films gives a refractive index of 1.14, which is, to the best of our knowledge, the lowest ever reported for TiO<sub>2</sub> films, corresponding to a pore volume of 92.5% (sorption behavior of the TiO<sub>2</sub> films investigated by ellipsometry will be discussed later on).

Interestingly, the inorganic precursor plays a crucial role in holding the integrity of the ridges during calcination. The ridges made solely of PS melt and flow, forming homogenous crack-free films (Figure S12b). Whereas with the TiO<sub>2</sub> precursor, the polymer still melts but the composite does not spread. This explains the behaviour of the film containing a low amount of TiO<sub>2</sub> during thermal treatment, and the necessity to have a certain amount of precursor to preserve the pattern. The shrinkage and the final shape of the ridges are not constant, and depend on the initial thickness of the film (and therefore on crack spacing as well). While the buckling accompanies the contraction of the thicker films, thinner ones are free of this effect. Buckling occurs due to inhomogeneous shrinkage: the top of the film contracts, where the bottom of the film is constrained by attachment to the substrate. When shrinkage varies too significantly between the top and bottom of the film, due to higher film thicknesses, buckling is observed. Moreover, thinner films exhibit much lower lateral shrinkage compared to thicker ones. The schematic in **Figure 2C** summarizes the discussed effects of withdrawal speed and calcination temperature on the crack spacing, shrinkage and buckling. An additional parameter for tuning the features of micropatterns is the heating rate. Low heating ramps effectively minimize buckling and reduce the crack width (Figure S15).

## 2.2. Chemical versatility

Latex colloids stabilized by nonionic surfactants are effective and versatile templating and cracking agents, forming stable aqueous inks with various molecular (e.g. alkoxides,  $\beta$ -diketonates) and ionic species (simple salts e.g. chloride, nitrates, acetates; or polyionic salts e.g. metatungstates). They

enable, therefore, direct patterning of inorganic films of different chemical nature and functionalities as simple oxides  $\text{TiO}_2$ ,  $\text{SiO}_2$ ,  $\text{ZrO}_2$ ,  $\text{Ga}_2\text{O}_3$ ,  $\text{IrO}_2$ ,  $\text{RuO}_2$ ,  $\text{WO}_3$ ,  $\text{V}_2\text{O}_5$ ; doped oxides  $\text{Sn}:\text{In}_2\text{O}_3$  (ITO), refractory binary oxides  $\text{CoTiO}_3/\text{Co}_2\text{TiO}_4$  and even metals Ir and Ru (**Figure 3**). After the deposition, each film exhibits the same features of unidirectional and evenly spaced cracks (Figure S16), the same as in the case of pure latex. The films are homogenous over a cm-size area, without secondary cracks, irrespective of the inorganic precursor used. The co-deposited inorganics can condense (sol-gel precursors) or simply crystallize in the colloidal network, providing enormous versatility to the method.

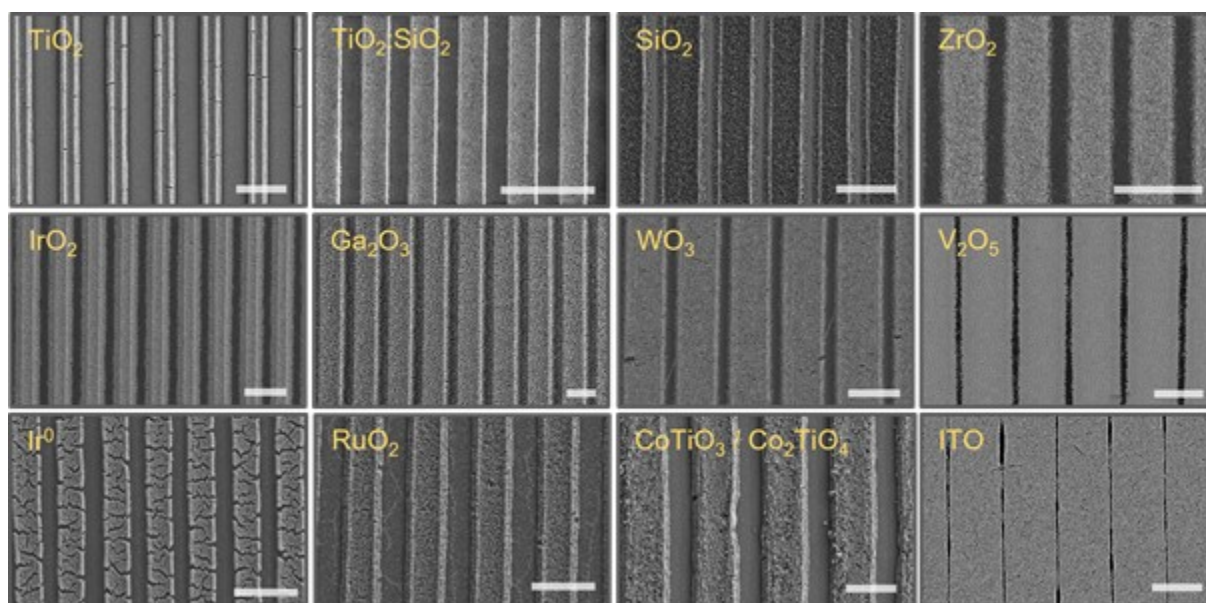


Figure 3. Tuning the composition of crack-patterned films. The SEM pictures of calcined crack-patterned films fabricated from inks containing different inorganic precursors; Each film is porous, the composition after calcination is indicated in the images. ITO stands for tin doped indium oxide. Scale bars represent 30  $\mu\text{m}$ .

Similar to  $\text{TiO}_2$ , subsequent calcination removes the polymeric templates and induces consolidation and crystallization of inorganic phases while keeping the micropattern architecture, as observed by SEM and optical microscopy (Figure 3, S16). While periodic grooves can be obtained for each material, the lateral width of the ridges and the final morphology is different (Figure 3, S17). This is related to the different volume shrinkage associated to the condensation (and crystallization) of the different sol-gel precursors. Interestingly, adding a small amount of silica precursor to titania ink strongly reduces shrinkage of the ridges during calcination (Figure 3  $\text{TiO}_2:\text{SiO}_2$ ), thus eliminating small

cracks in  $\text{TiO}_2$  ridges and enhancing quality of ridges. This is a trick already used in fabrication of mesoporous  $\text{TiO}_2$  films, avoiding crack formatting by impeding crystallization.<sup>[15]</sup> The different mechanism of condensation of the various inorganic precursors also results in a different porous structures. As show in Figure S17, all materials are highly porous. However, the size of pores are not always related to the diameter of PS latexes template. (Figure S17). It relates to the condensation, crystallization and physical behavior of inorganic precursors in respect to the thermal evolution of the polymer. For instance,  $\text{SiO}_2$  and  $\text{IrO}_2$  show porosity similar to  $\text{TiO}_2$ , while tungsten oxide exhibits a microporous sponge-like morphology. This is probably due to the fact that the precursor of  $\text{WO}_3$ , ammonium metatungstate, melts at a temperature similar to the glass transition of PS, causing phase separation during thermal treatment. As the consequence, the size of pores in  $\text{WO}_3$  films is not related to the size of latex particles.

Furthermore, we demonstrated that the polymeric latexes can also serve as reducing agents.<sup>[43]</sup> Indeed, calcination in an oxygen-free atmosphere forms micro-structured metallic iridium or ruthenium (**Figure 3**, S18-S19). In this case, the latex particles play the triple role of templating, cracking, and reducing agents. In contrast to other compositions, Ir and Ru ridges are cracked. The formation of small random cracks is due to very large volume shrinkage occurring during reduction. This is not surprising considering the large density increase upon crystallization of metallic phases (5.3 to 22.56  $\text{g cm}^{-3}$  in the case of Ir and from 3.11 to 12.2  $\text{g cm}^{-3}$  for Ru sample) All fabricated micropatterned films of different composition were crystalline as was confirmed by X-ray diffraction (XRD) analysis (Figure S20). We thus demonstrate that the self-ordering approach can be extended to numerous functional inorganic materials. However, controlling the nanoporosity and/or limiting the formation of small cracks in the ridge would require an optimization for each composition that goes beyond the scope of this work. This will include adjusting the formulation of the aqueous ink (such increasing the inorganic/inorganic ratio) or the annealing step." Nevertheless, the selected chemical compositions cover a wide spectrum of properties, including insulating ( $\text{SiO}_2$ ,  $\text{ZrO}_2$ ,  $\text{Ga}_2\text{O}_3$ ),<sup>[44]</sup> photoactive ( $\text{TiO}_2$ ,  $\text{CoTiO}_3$ ),<sup>[45]</sup> conductive (ITO, Ru, Ir),<sup>[46]</sup> electrocatalytic ( $\text{RuO}_2$ ,  $\text{IrO}_2$ ),<sup>[47]</sup> electrochromic materials ( $\text{WO}_3$ )<sup>[48]</sup> and cathodes for Li-ion batteries ( $\text{V}_2\text{O}_5$ )<sup>[49]</sup>.

### 2.3. 3D propagation of self-ordered cracks

In the following series of experiments, we explored the possibility of creating more sophisticated pattern geometries by transferring crack propagation to 3D space (out of plain) on multiple stacked layers. Once a film supported on a compliant substrate is subjected to a tensile strain, it may develop channeling cracks that propagate in plain and down into the substrate.<sup>[22]</sup> Drawing inspiration, we deposited the second layer from a pure solution of latex particles on the top of crack-patterned and non-calcined TiOR/PS, as shown in **Figure 4a**. The *in situ* optical microscopy revealed the formation of cracks in the upper layer that propagated down into the lower layer at a certain angle ( $\theta_{12}$ ), creating a square pattern (**Figure 4b**). **Figure 4c** shows the SEM image of the cross-section of this two-layer system. The red arrows indicate the cracks developed in the upper layer, which propagated down into the bottom layer. It means that the crack opening in the upper layer generated enough tensile stress in the lower layer for a new crack to form. The cracks from the bottom layer also translate to a subsequently deposited layer. In the **Figure 4d** they appear as thinner horizontal cracks. The bottom to top layer crack propagation depends primarily on the thickness of the upper layer. There are different modes at which all or each second crack propagates. For instance, Figure S21 shows the system made of two layers of pure PS latex in which we could observe that all cracks from the bottom layer were transferred to the upper one until the latter reached the thickness of about 3  $\mu\text{m}$ . Above this thickness more or less every second crack was translated to the upper layer (Figure S21).

Subsequent thermal treatment decomposes the latexes from both layers and induces contraction and crystallization of  $\text{TiO}_2$  (**Figure 4e**). In this case, the contraction occurs in two directions, yielding patterns of rectangular or rhomboidal features, depending on the angle between cracks. The size of the features is tuned in the same way as a single film by controlling the deposition speed. **Figure 4f** shows the SEM images of  $\text{TiO}_2$  patterns prepared with varying crack-angles between layers and the periodicity of the second layer. The shrinkage of the  $\text{TiO}_2$  rectangular features can be reduced by adding a small % of silica into the titania, either into the solution, or simply by exposing the non-calcined film to the vapours of silica precursors (such as MTMOS). In the latter case, the final features show larger dimensions, lower crack gap and less structural deformation (Figure S22).

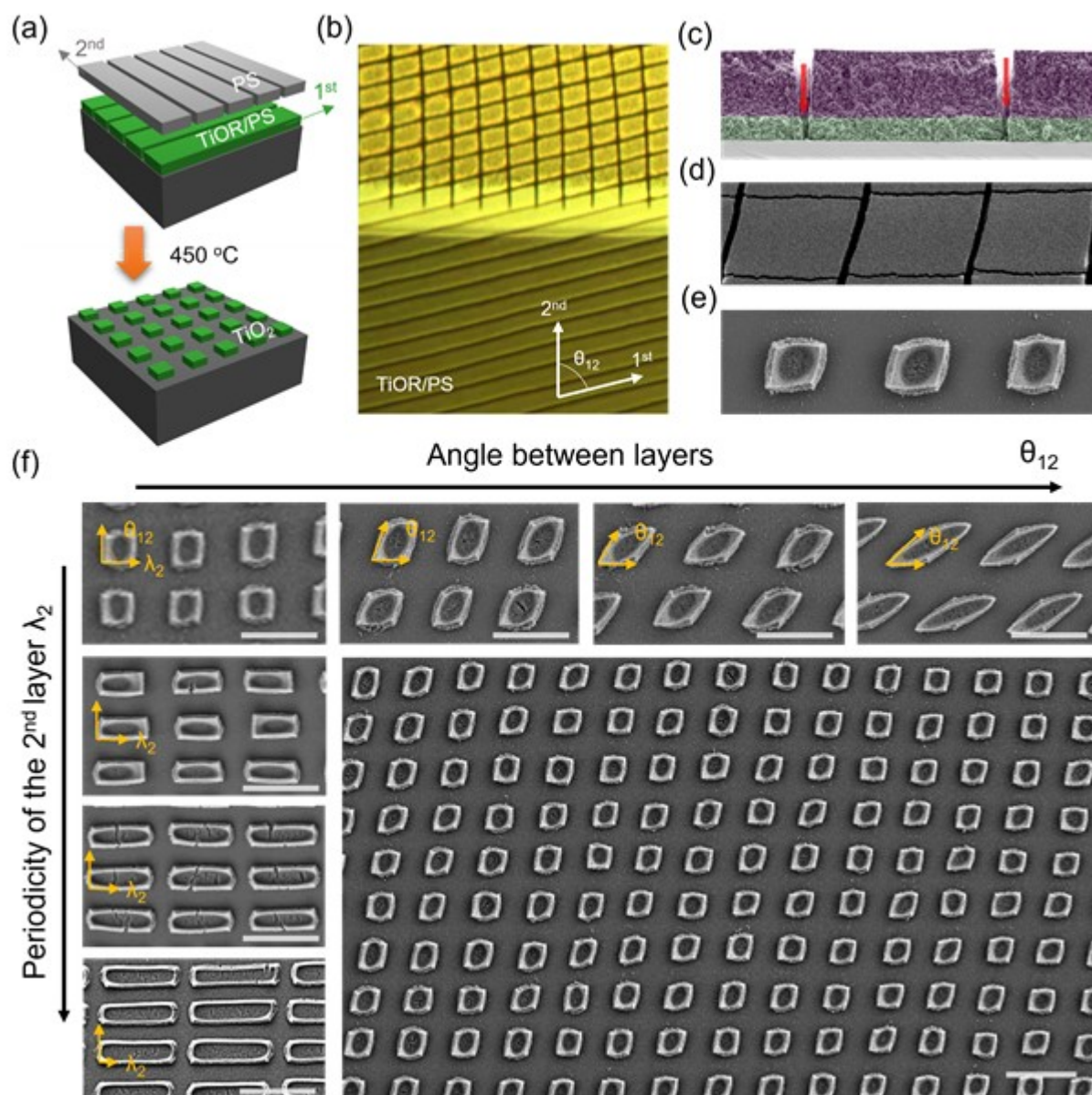


**Figure 4. Crack propagation in two layers system made of PS over TiOR/PS – tuning the type of pattern.** (a) Schematic of the formation of a second population of cracks in the TiOR/PS films, by depositing a second layer of pure PS latex particles to form square-like features upon calcination. (b) Optical microscopy image showing the propagation of cracks in the PS film deposited above the crack patterned TiOR/PS. (c) SEM cross-sectional image of two layers system of PS (violet) and TiOR/PS (green) presenting downward crack propagation, marked with red arrows. (d) SEM image of the top view of a two-layered system before calcination. The horizontal cracks originate from upward crack propagation. (e) Square-like TiO<sub>2</sub> patterns formed upon calcination of a PS on TiOR/PS two-layer system. (f) The modulation of the pattern features by changing the crack-spacing of upper

film ( $\lambda_2$ ) and the angle between cracks from 1<sup>st</sup> and 2<sup>nd</sup> layer  $\theta_{12}$ , the SEM images show titania patterns after flash calcination at 450 °C. Scale bars represent 30  $\mu\text{m}$ .

This approach can be further implemented toward heterostructures by using another ink containing an inorganic precursor to form the upper layer. To demonstrate, we fabricated a two-layer system with a bottom layer made of an ink of  $\text{ZrO}(\text{NO}_3)_2$  and PS latex colloids (ZrNO/PS) and a top layer of TiOR/PS, with cracks intersecting at 90° (**Figure 5a**). The thermal treatment produced a pattern with uniform Janus square features of  $\text{ZrO}_2$ , covered with  $\text{TiO}_2$ , as observed in the SEM images and confirmed by SEM EDX mapping (**Figure 5b**). High magnification shows the distinct pore structure (Figure S23). In addition, EDX analysis shows the differing chemical composition between the upper and lower layers, confirming the Janus character.

A crack pattern can also be conferred to a non-cracked continuous film, by depositing a PS ink as a second layer (**Figure 5c and d**). As discussed above, the strain developed in the upper layer can be transferred to a lower layer. This allows a decoupling of the crack spacing and the thickness of the films to produce a thin micropatterned inorganic film. In this case, the crack spacing in the lower film depends only on the crack spacing of the upper layer. The low thickness of the TiOR/PS induced minimal shrinkage and avoided buckling upon heat treatment. The film showed macroscopic homogeneity and high optical transparency (Figure S24). The cracks can propagate down through more than one layer. Two layers of cracking PS films were deposited on the top of thin non-cracked TiOR/PS. Cross-sectional SEM images confirms that cracks generated in the third layer smoothly propagated down to the first layer (Figure S25). This method, here used to create a square pattern in a previously continuous film is a promising way to create 2D structures and could perhaps be extended to other materials, otherwise incompatible with the PS latex formulation.

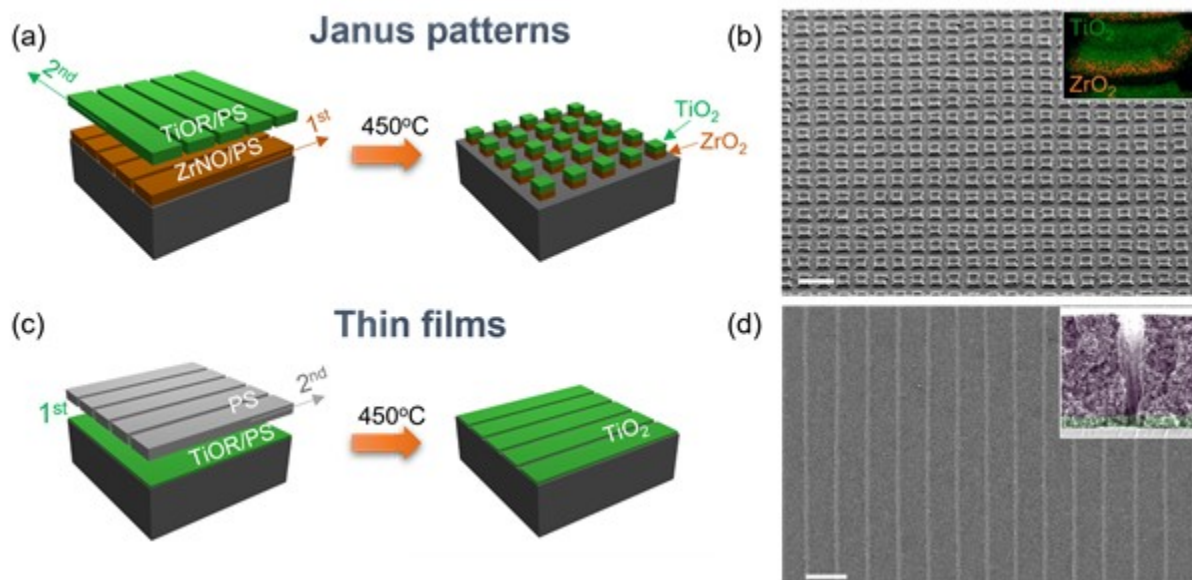


**Figure 5. Janus patterns and thin films.** (a) Schematic of the fabrication of square Janus features composed of  $\text{TiO}_2$  on top of  $\text{ZrO}_2$  and (b) the corresponding SEM image. The scale bar represents  $40\ \mu\text{m}$ . The inset shows EDX mapping of Ti (red) and Zr (green) elements. (c) Schematic of the fabrication of unidirectional crack pattern in thin  $\text{TiO}_2$  films and (d) the corresponding SEM image. The scale bar represents  $25\ \mu\text{m}$ . The inset shows the cross-section before calcination; two colours represents different layers (green being  $\text{TiO}_2$  and orange being  $\text{ZrO}_2$ ).

#### 2.4. Cracked films as temperature responsive photonic sensors

This simple method based on crack self-assembly allows the straightforward fabrication of tunable photonic components made of ultraporous materials. The highly periodic structure acts as diffraction gratings, which split and diffract light into several beams travelling in different directions (**Figure 6a**), and demonstrated by the diffraction of a beam from a red laser pointer (**Figure 6b**). The presence of several rainbow-colored patterns (**Figure 1e**), indicates that light is angularly diffracted and split into several diffraction orders. This dispersive capability of a crack-patterned films coated on silicon was probed by spectroscopic measurements in the reflectance mode for porous  $\text{TiO}_2$  films templated by  $65\ \text{nm}$  PS latexes and heat treated at  $450\ ^\circ\text{C}$ . As illustrated in **Figure 6a**, the reflection spectra were recorded by tilting the sample while keeping the position of the light source and the detector fixed. The 2D pattern in **Figure 6c** displays the evolution of reflectance spectra as function of the tilting angle  $\theta$  of a diffraction grating having periodicity of  $26.6\ \mu\text{m}$  (obtained by dip-coating at

0.005 mm s<sup>-1</sup>), as determined by AFM (Figure S26). The data are plotted as an image with vertical columns corresponding to spectra measured at each detection angle, and rows corresponding to the wavelengths detected by the spectrometer while the intensity of the reflected light is color-coded. The periodic structure shows three diffraction orders, visible as straight lines in the plot. This experimental trend is in good agreement with the theory (dotted lines), as determined by the grating equation (1) in this configuration:

$$\lambda = \frac{\sqrt{2}}{m} d \sin \vartheta \quad (1)$$

where  $\lambda$  is the wavelength,  $d$  is the grating periodicity,  $\vartheta$  is the tilting angle and  $m$  is the diffraction order (0,1,2,3...). Since the optical properties of the gratings depend on the crack periodicity, these can be tuned by controlling the withdrawal speed during dip-coating. Another example is shown in Figure S27, in which diffraction gratings with smaller periodicity (16.6  $\mu\text{m}$ ) were obtained by dip coating at a faster withdrawal rate 0.006 mm s<sup>-1</sup>. Here again, the 2D angle-resolved reflectance measurements highlight that the sample performs as a diffraction grating, but with light dispersion at higher angles, in agreement with the theory. The high porosity of these materials allows for engineering of the photonic device response.

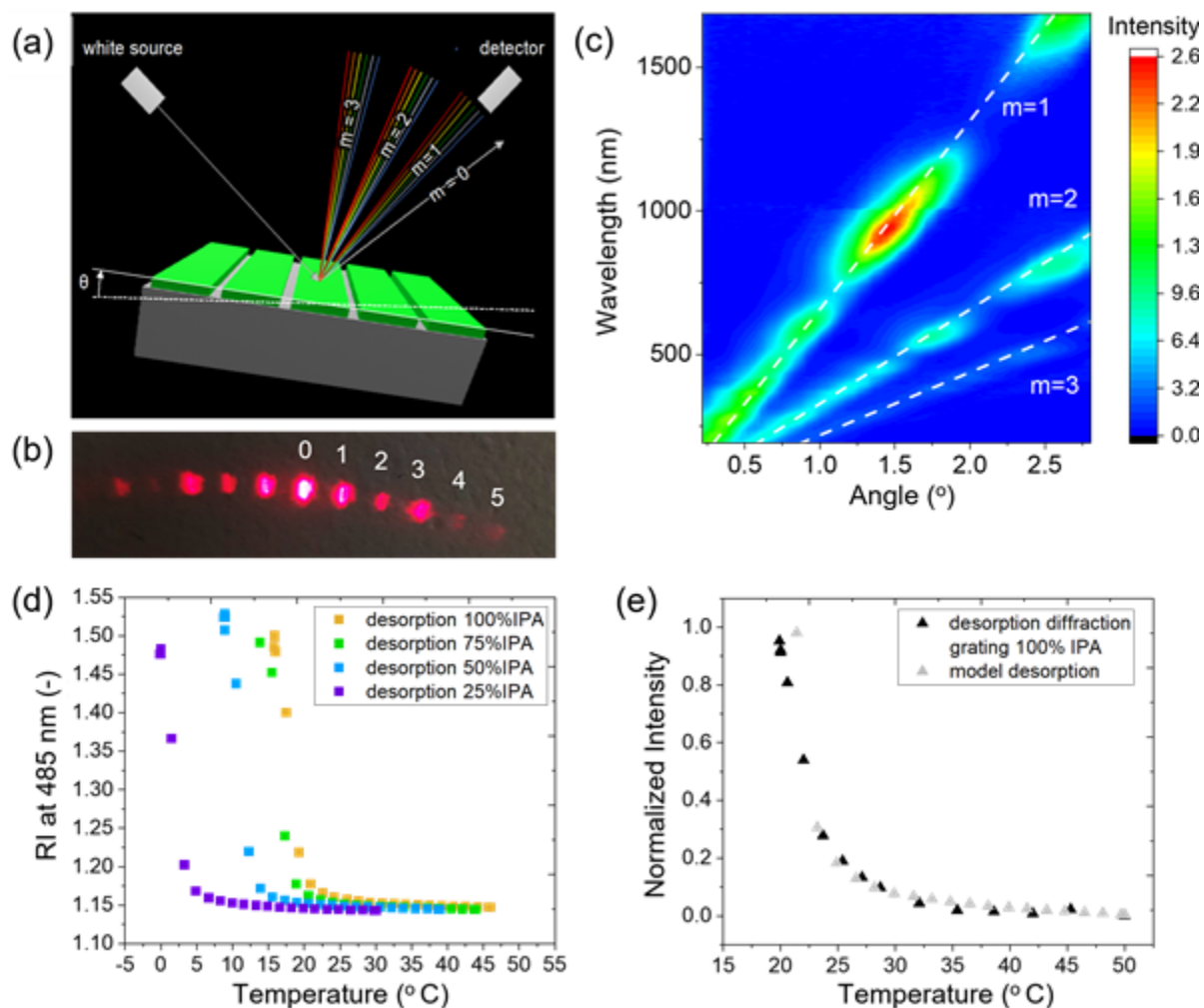


**Figure 6. Photonic grating sensor.** (a) Illustration of the angle-resolved spectroscopic characterization of crack-patterned diffraction gratings. (b) Diffraction grating performance of  $\text{TiO}_2$  crack-pattern films visualised in reflection mode with a red laser pointer. (c) Evolution of the reflectance spectra as a function of the tilting angle of a crack-patterned nanoporous  $\text{TiO}_2$  diffraction grating, represented in two dimensions by plotting the tilting angle versus the wavelength, with the intensity represented by colour code. Dotted lines represent the theoretical trends calculated based on grating parameters. (d) In-situ ellipsometry: evolution of the refractive index of a thin  $\text{TiO}_2$  porous film (without cracks) versus temperature at different isopropanol partial pressures ( $P/P_0$ ). (e) Experimental and theoretical evolution of the normalized diffracted intensity (first-order) as a function of the temperature for a  $\text{TiO}_2$  porous crack patterned diffraction grating.

A temperature responsive diffraction grating sensor is created from these materials. The signal transduction relies on the diffraction intensity variation in response to temperature variation. In particular, we exploit the liquid-to vapor phase transition taking place in mesopores caused by temperature variation. The porous TiO<sub>2</sub> diffraction grating is placed in a closed chamber in the presence of isopropyl alcohol (IPA) vapors at a controlled vapor pressure ( $P/P_0$ ). Two extreme cases can be identified: (i) at a low temperature, capillary condensation takes place and the alcohol is in the liquid phase in the pores; (ii) at high temperature, desorption occurs leaving the pores filled with air. From this relatively simple phase transition, we can engineer a versatile thermo-optical mechanism in which the optical properties vary significantly with the temperature. To show that, we first investigated a thin TiO<sub>2</sub> porous film without cracks by in-situ ellipsometry. **Figure 6d** displays the evolution of the refractive index at 485 nm as function of the temperature for different isopropanol partial pressures ( $P/P_0$ ), precisely controlled by a flow meter. In this example, we show the desorption curves while adsorption and thickness evolution are reported in Figure S28. In the case of a saturated atmosphere ( $P/P_0=100\%$ ), the increase in temperature causes a sharp decrease in refractive index from 1.49 at 16 °C (IPA-filled porosity) to 1.14 at 25 °C (air-filled porosity). The thermal coefficient of the refractive index  $dn/dT$  between 16 °C and 25 °C (that defines the thermal sensitivity of a sensor) is  $-0.039\text{ K}^{-1}$ . As a comparison, this value is two and three orders of magnitude higher than the temperature-induced refractive index variation of poly(methyl methacrylate), and dense TiO<sub>2</sub> respectively<sup>[50]</sup> over a similar temperature range.<sup>[51]</sup> The thermal sensitivity of the porous crack-patterned gratings is of the same order of magnitude of ZIF-8 photonic balls in presence of EtOH vapors.<sup>[50]</sup> Notably, as shown in Figure 6d, the  $n/T$  curves at lower IPA  $P/P_0$  (75%, 50% and 25%) present the same sensitivity, but are displaced toward lower temperature. From an applicative point of view, this indicates that the detection range can also be tuned on-demand by controlling the atmosphere around the material, or by changing the vapor molecule (i.e. less volatile molecules desorb at higher temperatures). We then apply the same principle to the crack patterned diffraction grating characterized previously in Figure S27 having a thickness of around 1  $\mu\text{m}$  and a periodicity equal to 16.6  $\mu\text{m}$ . In this study, we mainly monitored the 1<sup>st</sup> order diffraction intensity ( $I_1$ ) at 485 nm (consistent with previous ellipsometry analysis). Figure 6e displays the evolution of the normalized intensity of the  $I_1$  as a function of the temperature in an atmosphere of  $P/P_{0\text{ IPA}}=100\%$ . The temperature-induced desorption from the TiO<sub>2</sub> pores causes a decrease of the refractive index and of the intensity of the diffracted light. This trend is not always linear and can be verified semi-empirically following models proposed by Whitesides and co-workers for gratings made of arrays of

lines.<sup>[52,53]</sup> According to the theory, a phase difference ( $\varphi$ ) is created when light passes through the diffraction grating. The phase difference depends on the light wavelength  $\lambda$ , on the grating thickness  $h$ , and on the refractive index contrast between the diffraction grating film ( $n_{DG}$  – here it is porous  $\text{TiO}_2$ ) and the surrounding atmosphere ( $n_{\text{air}}=1$ ) and is given in Equation (2):

$$\text{—————} \quad (2)$$

The first order diffracted intensity can be deduced from  $\varphi$  and is given in Equation (3)

$$\text{—————} \quad (3)$$

Since both  $n_{DG}$  and  $h$  vary with temperature in the presence of IPA, we entered into the equation the value obtained by *in-situ* ellipsometry of the thin, not-cracked  $\text{TiO}_2$  film, as shown in **Figure 6d** and S28. **Figure 6e** confirms that the model is in very good agreement with the experimental trend, suggesting that this simple equation can be used to predict the sensor outcome and as a guide to the structural design of the device. Despite its simplicity, this example illustrates the potential of the scalable crack patterning of porous films for photonic and sensing applications.

### 3. Conclusions

By understanding the fundamentals of crack formation in inorganic-latex inks, we presented a general lithography-free micropatterning method for inorganic nanoporous films. The aqueous inks were subjected to a stress gradient upon directional drying, which guides cracks and induces self-ordering into well-defined unidirectional patterns. The method is highly versatile and led to the formation of numerous nanoporous films of simple and binary metal oxides and noble metals covering a whole spectrum of properties including insulator, photocatalytic, electrocatalytic,

conductive, electrochromic materials. Such flexibility came from nonionic surfactants stabilizing latex particles in solution and most likely interacting with inorganic precursors on the latex surface. Engineering multilayer stacks allowed us to direct crack formation not only in-plane, but also out of plane, between the layers, and achieving higher levels of geometrical control. This enabled the fabrication of polygonal micropatterns with tunable shapes, sizes of the features and multiple compositions (including Janus patterns). The porous films with self-ordered cracks diffract light and can be used as thermo-optical photonic sensors.

Drying aqueous inks offers key advantages with respect to conventional lithographic methods for the fabrication of inorganic patterned films: (i) it is cost-effective and it does not require sophisticated equipment since patterning takes place directly during deposition; (ii) it is compatible with various meniscus-guided deposition techniques (such as dip-coating, blade-coating or drop-casting) enabling direct deposition and patterning at speed up to  $1 \text{ mm s}^{-1}$  by solution shearing process on preheated substrates (Figure S29); (iii) the approach is extremely chemically versatile and it enables direct integration of numerous porous inorganic materials into periodic structures; (iv) compared to conventional lithographic resists, the aqueous inks reported in this study are environmental friendly, non-toxic, chemically stable and easily recyclable, all key advantages toward the future industrialization of the process; and (v) patterned inorganic surfaces can be fabricated over large scale surfaces by using methods (such as dip-coating) that enable deposition and patterning on non-planar supports such as cylindrical supports (Figure S30). For all the aforementioned reasons, the method opens perspectives for applications of solution-processed inorganic materials in a number of applications requiring patterning on large-scale such as solar cells, wetting, photonics. More broadly, the self-ordering of cracks represents a unique example of robust self-assembly with long-range order.

### **Supporting Information**

Supporting Information is available from the Wiley Online Library or from the author.

### **Acknowledgements**

M.F. and F.T. acknowledges funding from the European Research Council (ERC) under European Union's Horizon 2020 Programme (Grant Agreement no. 803220, TEMPORE). M.O. acknowledges College de France for financial support and the Foundation for Polish Science (FNP) for a START scholarship.

Received: ((will be filled in by the editorial staff))

Revised: ((will be filled in by the editorial staff))

Published online: ((will be filled in by the editorial staff))

- [1] R. Zhu, C. Y. Jiang, B. Liu, S. Ramakrishna, *Adv. Mater.* **2009**, *21*, 994.
- [2] A. Barranco, A. Borrás, A. R. Gonzalez-Elipé, A. Palmero, *Prog. Mater. Sci.* **2016**, *76*, 59.
- [3] M. T. Colomer, *Adv. Mater.* **2006**, *18*, 371.
- [4] C. Li, M. Iqbal, J. Lin, X. Luo, B. Jiang, V. Malgras, K. C. W. Wu, J. Kim, Y. Yamauchi, *Acc. Chem. Res.* **2018**, *51*, 1764.
- [5] C. Li, Ö. Dag, T. D. Dao, T. Nagao, Y. Sakamoto, T. Kimura, O. Terasaki, Y. Yamauchi, *Nat. Commun.* **2015**, *6*, 6608.
- [6] B. Smarsly, M. Antonietti, *Eur. J. Inorg. Chem.* **2006**, 1111.
- [7] Z. Shen, D. M. O'Carroll, *Adv. Funct. Mater.* **2015**, *25*, 3302.
- [8] M. Faustini, A. Cattoni, J. Peron, C. Boissière, P. Ebrard, A. Malchère, P. Steyer, D. Grosso, *ACS Nano* **2018**, *12*, 3243.
- [9] X. Yao, Y. Hu, A. Grinthal, T. S. Wong, L. Mahadevan, J. Aizenberg, *Nat. Mater.* **2013**, *12*, 529.
- [10] C. Howell, A. Grinthal, S. Sunny, M. Aizenberg, J. Aizenberg, *Adv. Mater.* **2018**, *30*, 1802724(1).
- [11] E. Lancelle-Beltran, P. Prené, C. Boscher, P. Belleville, P. Buvat, S. Lambert, F. Guillet, C. Boissière, D. Grosso, C. Sanchez, *Chem. Mater.* **2006**, *18*, 6152.
- [12] C. Sanchez, C. Boissière, D. Grosso, C. Laberty, L. Nicole, *Chem. Mater.* **2008**, *20*, 682.

- [13] D. Grosso, C. Boissiere, B. Smarsly, T. Brezesinski, N. Pinna, P. A. Albouy, H. Amenitsch, M. Antonietti, C. Sanchez, *Nat. Mater.* **2004**, *3*, 787.
- [14] D. Grosso, C. Boissière, L. Nicole, C. Sanchez, *J. Sol-Gel Sci. Technol.* **2006**, *40*, 141.
- [15] M. Faustini, A. Grenier, G. Naudin, R. Li, D. Grosso, *Nanoscale* **2015**, *7*, 19419.
- [16] P. Falcaro, L. Malfatti, L. Vaccari, H. Amenitsch, B. Marmiroli, G. Greci, P. Innocenzi, *Adv. Mater.* **2009**, *21*, 4932.
- [17] H. Uchiyama, M. Hayashi, H. Kozuka, *RSC Adv.* **2012**, *2*, 467.
- [18] J. Gao, S. Semlali, J. Hunel, D. Montero, Y. Battie, D. Gonzalez-Rodriguez, R. Oda, G. L. Drisko, E. Pouget, *Chem. Mater.* **2020**, *32*, 821.
- [19] M. Takahashi, T. Maeda, K. Uemura, J. Yao, Y. Tokuda, T. Yoko, H. Kaji, A. Marcelli, P. Innocenzi, *Adv. Mater.* **2007**, *19*, 4343.
- [20] B. Ai, H. Möhwald, D. Wang, G. Zhang, *Adv. Mater. Interfaces* **2017**, *4*, 1600271.
- [21] K. H. Nam, I. H. Park, S. H. Ko, *Nature* **2012**, *485*, 221
- [22] M. Kim, D. Ha, T. Kim, *Nat. Commun.* **2015**, *6*, 1.
- [23] L. Guo, Y. Ren, L. Y. Kong, W. K. Chim, S. Y. Chiam, *Nat. Commun.* **2016**, *7*, 1.
- [24] J. Jung, K. K. Kim, Y. D. Suh, S. Hong, J. Yeo, S. H. Ko, *Nanoscale Horizons* **2020**, *5*, 1036.
- [25] H. Kim, M. K. Abdelrahman, J. Choi, H. Kim, J. Maeng, S. Wang, M. Javed, L. K. Rivera-Tarazona, H. Lee, S. H. Ko, T. H. Ware, *Adv. Mater.* **2021**, *33*, 1.
- [26] C. Allain, L. Limat, *Phys. Rev. Lett.* **1995**, *74*, 2981.
- [27] W. Han, B. Li, Z. Lin, *ACS Nano* **2013**, *7*, 6079.
- [28] B. Li, B. Jiang, W. Han, M. He, X. Li, W. Wang, S. W. Hong, M. Byun, S. Lin, Z. Lin, *Angew. Chemie - Int. Ed.* **2017**, *56*, 4554.
- [29] O. Dalstein, E. Gkaniatsou, C. Sicard, O. Sel, H. Perrot, C. Serre, C. Boissière, M. Faustini, *Angew. Chemie - Int. Ed.* **2017**, *56*, 14011.

- [30] B. Hatton, L. Mishchenko, S. Davis, K. H. Sandhage, J. Aizenberg, *Proc. Natl. Acad. Sci. U. S. A.* **2010**, *107*, 10354.
- [31] K. R. Phillips, G. T. England, S. Sunny, E. Shirman, T. Shirman, N. Vogel, J. Aizenberg, *Chem. Soc. Rev.* **2016**, *45*, 281.
- [32] Y. J. Kim, M. H. Lee, H. J. Kim, G. Lim, Y. S. Choi, N. G. Park, K. Kim, W. I. Lee, *Adv. Mater.* **2009**, *21*, 3668.
- [33] B. O'Regan, M. Gratzel, *Nature* **1991**, *353*, 737.
- [34] K. Nakata, A. Fujishima, *J. Photochem. Photobiol. C Photochem. Rev.* **2012**, *13*, 169.
- [35] Q. Guo, C. Zhou, Z. Ma, X. Yang, *Adv. Mater.* **2019**, *31*, 1901997 (1).
- [36] E. Scolan, C. Sanchez, *Chem. Mater.* **1998**, *10*, 3217.
- [37] X. Gu, L. Shaw, K. Gu, M. F. Toney, Z. Bao, *Nat. Commun.* **2018**, *9*, 534(1).
- [38] M. Faustini, B. Louis, P. A. Albouy, M. Kuemmel, D. Grosso, *J. Phys. Chem. C* **2010**, *114*, 7637.
- [39] K. A. Shorlin, J. R. De Bruyn, M. Graham, S. W. Morris, *Phys. Rev. E* **2000**, *61*, 6950.
- [40] L. Rozes, C. Sanchez, *Chem. Soc. Rev.* **2011**, *40*, 1006.
- [41] D. Grosso, *J. Mater. Chem.* **2011**, *21*, 17033.
- [42] E. Bindini, G. Naudin, M. Faustini, D. Grosso, C. Boissière, *J. Phys. Chem. C* **2017**, *121*, 14572.
- [43] M. Odziomek, M. Bahri, C. Boissiere, C. Sanchez, B. Lassalle-Kaiser, A. Zitolo, O. Ersen, S. Nowak, C. Tard, M. Giraud, M. Faustini, J. Peron, *Mater. Horizons* **2020**, *7*, 541.
- [44] M. Grobis, C. Schulze, M. Faustini, D. Grosso, O. Hellwig, D. Makarov, M. Albrecht, *Appl. Phys. Lett.* **2011**, *98*, 192504.
- [45] R. Li, M. Faustini, C. Boissière, D. Grosso, *J. Phys. Chem. C* **2014**, *118*, 17710.
- [46] M. J. Alam, D. C. Cameron, *Thin Solid Films* **2000**, *377–378*, 455.
- [47] M. Elmaalouf, M. Odziomek, S. Duran, M. Gayrard, M. Bahri, C. Tard, A. Zitolo, B. Lassalle-Kaiser, J. Y. Piquemal, O. Ersen, C. Boissière, C. Sanchez, M. Giraud, M. Faustini, J. Peron, *Nat.*

- Commun.* **2021**, *12*, 3935.
- [48] P. Judeinstein, J. Livage, *J. Mater. Chem.* **1991**, *1*, 621.
- [49] Y. Yue, H. Liang, *Adv. Energy Mater.* **2017**, *7*, 1602545.
- [50] T. Toyoda, M. Yabe, *J. Phys. D. Appl. Phys.* **1983**, *16*, L251.
- [51] C. Avci, M.L. De Marco, C. Byun, J. Perrin, M. Scheel, C. Boissière, M. Faustini, *Adv. Mater.*, **2021** *33*(43), 2104450
- [52] O. J. A. Schueller, D. C. Duffy, J. A. Rogers, S. T. Brittain, G. M. Whitesides, *Sensors Actuators, A Phys.* **1999**, *78*, 149.
- [53] B. A. Grzybowski, D. Qin, G. M. Whitesides, *Appl. Opt.* **1999**, *38*, 2997.